PHYSICAL REVIEW E **72**, 056310 (2005)

MRI measurements of an acoustically cavitated fluid in a standing wave

Igor V. Mastikhin* and Benedict Newling
MRI Centre, Department of Physics, P.O. Box 4400, University of New Brunswick, Fredericton, New Brunswick, Canada E3B 5A3

(Received 22 June 2005; published 8 November 2005)

Magnetic resonance imaging was applied to studies of cavitating fluid in a standing acoustic wave at 31 kHz sound frequency. A spin-echo pulsed field gradient sequence was employed to sensitize the measurement to motion. Velocity spectra, kinetic energy maps, and maps of the dispersion coefficient were obtained for pure water, water with surfactant (sodium dodecyl sulfate, 1 m*M*), and water with sodium dodecyl sulfate–NaCl ([NaCl]=0.1*M*). Cavitation bubbles cause an increase in dispersion coefficient and acoustic streaming. These effects are not observed in a degassed sample. Streaming was most developed in samples with surfactants, which also demonstrate a pronounced anisotropy of the dispersion coefficients parallel and normal to the direction of the sound wave propagation. Stabilization of the bubble surface and concomitant reduction of bubble coalescence by the surfactant can explain the observed differences.

DOI: 10.1103/PhysRevE.72.056310 PACS number(s): 47.55.Bx, 76.60.Pc, 43.25.+y

I. INTRODUCTION

Acoustic cavitation is the generation, oscillation, and collapse of gaseous bubbles in fluids under the action of high-power ultrasound. The prevalent methods used in studies of cavitation are optical and acoustical. By their nature, these techniques are sensitive to changes in optical or acoustical transparency, respectively. The bubbles in a cavitating fluid reflect light and absorb and reradiate acoustic signals. The shielding effect of surrounding bubbles makes it difficult to obtain information about the central zones of a cavitation cloud.

In this work, we apply magnetic resonance imaging (MRI) methods to the study of a cavitating fluid. The MRI signal is an electromotive force induced in the receiver coil by the coherent precession of many sample nuclei around an externally applied magnetic field. MRI methods are very flexible, because many physical factors may modulate the MRI signal, thus providing us with information on various physicochemical parameters of the sample such as viscosity, velocity, diffusion, and molecular density. Linear gradients of magnetic field allow spatial resolution of such information in three dimensions, noninvasively and from an optoacoustically opaque medium.

Cavitation phenomena cover a very wide time scale, from subnanoseconds (the duration of a single flash of light from a collapsing bubble), to microseconds (a bubble oscillation period), to milliseconds, seconds, and minutes (bubble interaction, rectified diffusion, and fluid heat transfer). MRI methods can never deliver millions of frames per second, as optical methods can. The fastest one-dimensional MRI acquisition cannot be made shorter than a fraction of a millisecond. However, MRI is able to measure processes on the time scale of milliseconds and seconds, providing statistically averaged information. We show the applicability of MRI to studies of the dynamics of a cavitating fluid, with spatially resolved measurements of velocity spectra and hydrodynamic dispersion coefficient.

Acoustic streaming is a bulk advective flow caused by attenuation of acoustic waves [1]. Such attenuation can occur due to the absorption of the sound energy by the fluid itself, or through the presence of absorbing agents such as bubbles. Therefore, measurements of acoustic streaming can provide information on the cavitation field [2]. A different kind of streaming, microstreaming, is a microflow in the vicinity of collapsing and fragmenting bubbles. Microstreaming actively mixes the fluid and thus contributes to the measured hydrodynamic dispersion coefficient of the fluid.

The measurements have been performed during the initial stage of degassing cavitation for pure water, degassed water, water with surfactants [sodium dodecyl sulfate (SDS)], and water with SDS and NaCl. It is known that surfactants modify the dynamics of a cavitating bubbles, affecting sonochemistry and sonoluminescence in the cavitation field [3,4]. We have investigated the surfactant modification of the dynamics of cavitating fluid on the macroscale.

The velocity measurements show markedly different streaming patterns. The dispersion maps also indicate changes in local mixing of the fluid. The results can be explained in terms of the modifying effects of surfactants on the coalescence of cavitating bubbles.

II. MATERIALS AND METHODS

All measurements were performed on a Nalorac (Martinez) 2.35 T, horizontal-bore superconducting magnet with a Tecmag (Houston) Apollo console. A water-cooled 20-cm-i.d. Nalorac magnetic field gradient set was driven by Techron (Elkhart) 8710 amplifiers. A quadrature birdcage radiofrequency (rf) coil (Morris) was driven by a 2 kW AMT (Brea) 3445 rf amplifier.

The 31 kHz Langevin-type ultrasonic transducer (SensorTech), with a parallel beam, was situated coaxially inside a 5-cm-i.d. 22-cm-long cylindrical vessel at the centre of the magnet (Fig. 1). In our experiments, we employed a transducer power of 3.48 W (measured by calorimetry, i.e., cal-

---

*Corresponding author. FAX: +506-453-4581. Email address: mast@unb.ca

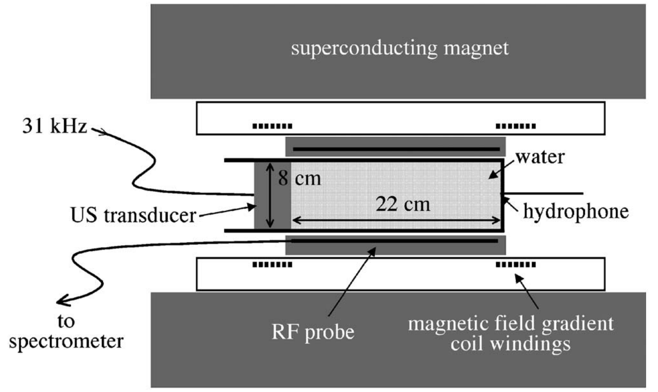

FIG. 1. The experimental setup. Ultrasound transducer is positioned inside rf probe and magnetic field gradient set. The direction of the main magnetic field B_0 is along the vessel axis.

culating power input by measuring the rate of temperature rise in the system, taking into account its thermal capacity). A standing wave condition, with nine half wavelengths, was established by reference to the hydrophone output. There was always a developed cavitation in the vessel (detected with a hydrophone) when the transducer was on. The vessel was aligned with the direction of the main magnetic field. Manganese sulfate (98.5%), SDS (>95%), and NaCl (99.5%) were purchased from Sigma-Aldrich. The water used to prepare all solutions was obtained from a Barnstead Nanopure purification system (Barnstead) and had a conductivity below 0.05 μS cm^{-1}.

Several different MRI methods were employed to examine the cavitation field. However, the aluminum cover of the transducer and the microphone within the image field of view caused severe distortions of MR images obtained by such fast imaging methods as EPI, RARE, and FLASH. A standard spin-echo imaging was found to be the most robust imaging method. Unfortunately, it was also the most time inefficient, forcing us to restrict spatial resolution to only one dimension in order to reduce imaging time.

All MRI data were acquired from ^{1}H of water at a MRI frequency of 99.2 MHz. All water solutions were doped with 0.2 mM of manganese sulfate to decrease the spin-lattice relaxation time of the proton MRI signal to 0.58 s and, thus, reduce the imaging time. If nothing else has been added to them, we will call such water solutions "pure water" from now on.

We employed a displacement-sensitive pulsed field gradient (PFG) sequence [5] with slice selection (Fig. 2). The PFG measurements of velocity are based on the principle of phase encoding. When nuclei (in our case, ^{1}H of water molecules) move in the presence of bipolar magnetic field gradients G, their MR signal phase becomes proportional to their mean velocity v over the time interval Δ between leading edges of the gradient pulses [5,6]:

$$\varphi(t) = \gamma \delta G \cdot v(\Delta - \delta/3) \quad (1)$$

where γ is the gyromagnetic ratio of the nucleus and δ is the duration of the gradient pulse. The gradient value is incremented and the measurement is repeated. After N data sets with different gradient values have been acquired, a Fourier transform is performed, and an N-point velocity spectrum is resolved.

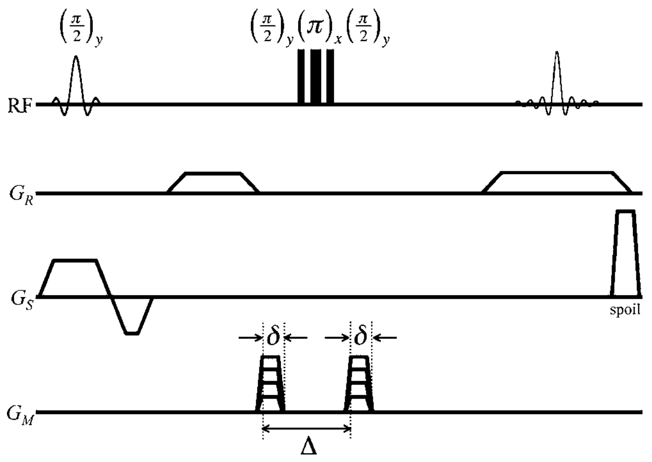

FIG. 2. Spin-echo pulse field gradient imaging sequence. The upper line is the history of rf pulse application and data acquisition. G_R and G_S lines show magnetic field gradients employed for spatial encoding and slice selection. G_M is a motion-sensitizing gradient which can be applied in an arbitrary direction.

The signal from spins flowing coherently in the direction of applied gradient will be shown in the spectrum as a peak centered at their velocity v. Molecular self-diffusion causes an attenuation of the PFG MRI signal (over the N measurements) as the stochastic motion imparts a phase dispersion to the collection of ^{1}H. In the velocity spectrum, self-diffusion determines the width of the velocity peak. Both velocity and diffusion information may be extracted from the same PFG measurement. The term "hydrodynamic dispersion" will be used here to include the effects of both molecular self-diffusion and kinematic dispersion—a stochastic element of the flow field which may arise from turbulence or the presence of a porous barrier to flow, for example. The effects of hydrodynamic dispersion upon the PFG MRI signal are the same as those of self-diffusion, although the broadening of the velocity peak may be more extreme. In turbulent flow, for example, a very broad spectral peak indicates a time averaged velocity and the width of the peak is indicative of the magnitude of velocity fluctuations in the direction of G. Stationary spins will not acquire the signal phase and will appear in the spectrum at zero. Thus we can use the PFG measurements to distinguish between a coherent motion of the fluid, a turbulent fluid motion, and an absence of motion.

A dispersion coefficient D is most readily extracted not from the width of the velocity spectrum, but from the MRI signal decay. Over N data sets, the obtained dispersion decays were fitted with monoexponential decay of the form

$$\frac{F}{F_0} = \exp[-\gamma^2 G^2 \delta^2 D(\Delta - \delta/3)]. \quad (2)$$

The fitted values of D with standard errors larger than 10% were rejected and replaced with zeros on the maps of dispersion coefficient. In this case, either local velocities were fluctuating rapidly on the time scale of the NMR measurement or bubble-induced local magnetic field inhomogeneities perturbed the MR signal. The discontinuity in magnetic susceptibility at an air/liquid boundary (bubble wall) gives rise to a local magnetic field inhomogeneity [6]. In either case, the exaggerated standard errors were indicators of an intense cavitation.

The PFG MRI parameters were as follows: the maximum gradient strength was 7.2 G/cm, δ=6 ms, Δ=20 ms, and N=32 gradient steps yielding a velocity resolution of 1.02 mm/s. The spatial resolution was 0.9 mm for profiles along the vessel axis and 0.35 mm for transverse profiles. Slice selection allowed acquisition of a signal only from a slice of the sample, if necessary. The orientation and position of the slice is completely controlled in the MRI acquisition. We employed two orientations: a coronal orientation, parallel to the axis of the cylinder and passing through the center of the vessel, and a transverse orientation, perpendicular to the axis of the vessel and passing through the middle of the vessel. The thickness of the slice was 1.9 cm.

With a repetition time of 0.5 s, each measurement took 20 s, determining the temporal resolution of our experiments. After the start of sonication, however, when the perturbation front was propagating through the liquid, the border between the perturbed and yet unperturbed liquid was clearly identified in the dispersion-weighted profiles within data sets. This time resolution allowed us to estimate the velocity of the initial perturbation during 5–15 s after the start of sonication.

The following data were calculated from the PFG measurements: maps of velocity, maps of stationary fraction of the fluid, kinetic energy maps, and maps of dispersion coefficient. To obtain maps of the stationary fraction of the fluids, the data from velocity spectra with velocities in the range from −1.02 to +1.02 mm/s (two bins next to the zero velocity) were extracted and normalized with respect to the first measurement in each series (for which the fluid was completely stationary):

$$I_{norm}(x_i,t)=\frac{I(x_i,t)}{I(x_i,0)}. \tag{3}$$

Kinetic energy maps were obtained from velocity spectra by multiplying the intensity of the spectral line by the square of the corresponding velocity and summing along the 32 points in the velocity dimension:

$$I_{energy}(x_i,t)=\sum_{-N/2}^{N/2} I(x_i,v_n,t)v_n^2. \tag{4}$$

For "positive" kinetic energy maps, only the positive half of the velocity spectrum ($n>0$) was summed.

Series of 32 PFG measurements were performed, requiring 10.6 min of the total experiment time. The ultrasonic transducer was activated after the fourth measurement in a series and turned off after the 25th. The series were acquired for degassed water, pure water, water with SDS, and water with SDS and NaCl. Data processing was performed with Interactive Data Language (RSI). Each series of measurements was performed more than three times, but not averaged. Only features observed in all three sets of experiments are discussed here.

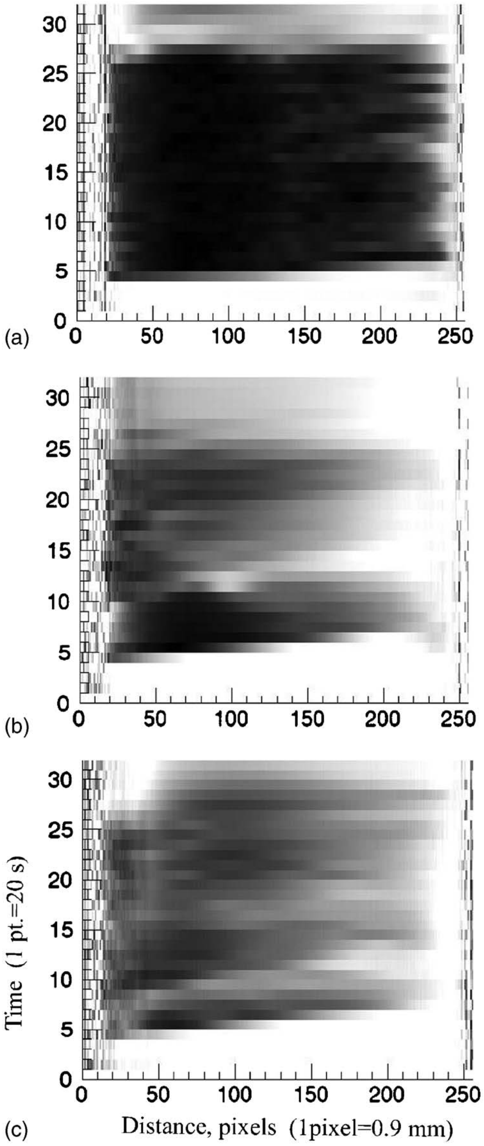

FIG. 3. Stationary fluid maps along the vessel axis for (a) pure water, (b) water with SDS, and (c) water with SDS-NaCl. The horizontal axis is distance along the vessel in pixels (1 pixel =0.9 mm), thus every row is a profile along the apparatus of Fig. 1, from the face of the ultrasound transducer at pixel 20 to the end of the vessel at pixel 242. The vertical axis is a time dimension in measurement number from a series of 32. Each measurement takes 20 s and the sonication takes place between measurements 5 and 25 inclusive. The gray scale represents volume fraction of stationary fluid at each position; the intensity runs from 0 (black, no stationary fluid) to 1 (white, no fluid motion).

III. RESULTS

A. Maps of stationary fluid in the whole vessel

The images in Fig. 3 show the amount of stationary fluid for pure water, water with SDS, and water with SDS-NaCl. Brighter pixels contain more stationary fluid. The data were acquired with no slice selection, so that the signal is a sum from the whole cross section of the vessel. The first (horizontal) dimension of each image is a spatial dimension oriented along the vessel axis, 0.9 mm per pixel. The second (vertical) dimension is the number of each measurement in the series of 32 PFG measurements acquired at 20 s intervals and, therefore, shows how the system evolves with sonication. Recall that the US transducer (which is to the left in the image) is activated after the fourth measurement (row 4).

20 s after the start of sonication, no stationary fluid is left in the pure water. The fluid along the whole vessel length is in motion. There is also a very short transition time from moving fluid to the stationary fluid after the ultrasound is turned off in row 25.

For water with SDS, the amount of stationary fluid is significantly greater through sonication. Initially water is more perturbed near the transducer, but quiescent near the opposite end of the vessel. It takes 20–40 s longer to perturb water along the whole length of the vessel than in the pure water case. Rather noticeable also is a periodic behavior of the perturbation: after the initial burst propagating through the whole length, the fluid becomes much quieter for about a minute, then another, weaker burst develops.

In the case of water with SDS-NaCl, there is much more stationary fluid than for pure water and water with SDS. The bursts perturb less water than in the other cases, but occur more frequently than in water with SDS. After the ultrasound is off, the water near the transducer becomes quiet at once, but the rest of the vessel is still in motion, unlike in the other cases. The density of the salted water is 5% higher than that of pure water, and inertia may play a role.

These observations agree with measurements of the perturbation front velocity from dispersion-weighted profiles, as explained in Sec. II (and shown in Sec. III C), during 5–15 s after the start of sonication. The measurements gave mean velocities of 14.4 ± 2.5 mm/s for the perturbation front in the pure water, 9 ± 0.4 mm/s for the front in the water with SDS, and 8.7 ± 0.8 mm/s for the front in the water with SDS-NaCl.

Analysis of the amount of stationary fluid tells us how much fluid is involved in turbulent and coherent motions, but it cannot distinguish between the two. To separate the contribution of a coherent flow of the fluid, we must analyze velocity spectra and kinetic energy maps.

B. Velocity spectra and kinetic energy maps

In Figs. 4(a)–4(f), velocity spectra of the fifth and sixth measurements (20 and 40 s after the start of sonication) are shown for the pure water, water with SDS, and water with SDS-NaCl. In this case, each image represents a single time point in the $N=32$ series of PFG measurements. The horizontal axis is the spatial dimension along the vessel; the vertical axis represents the velocity. The direction of the displacement encoding was chosen to be along the vessel axis. Positive velocities are above the central line of zero velocity and correspond to the displacement away from the transducer. Negative velocities appear below the central line and indicate counterflow, toward the transducer. The flow propagation along the vessel is clearly seen.

For the pure water, an initial coherent flow with wide distribution of velocities [Fig. 4(a)] disappears 20 s later next to the transducer [Fig. 4(b)]. Both positive and negative velocities are present next to the transducer, indicating the appearance of both the flow and counterflow. A region of coherent flow propagates along the vessel but is followed by a loss of coherence, as would be expected for a region of turbulence. Periodic oscillations in signal intensity near the high-intensity regions are artifacts, caused by the flow changing during the measurement. For the water with SDS, a steadier flow pattern, with well-defined flow and counterflow, indicating the presence of a circulation [Figs. 4(c) and 4(d)] is observed.

The water with SDS-NaCl demonstrates a similar, but weaker, flow with counterflow [Figs. 4(e) and 4(f)]. The negative (counterflow) velocities below the central line of zero velocity have smaller magnitude than for the other solutions, but they extend a similar distance along the vessel to those observed in water with SDS [Fig. 4(e)] c. 110 pixels and [Fig. 4(f)] c. 160 pixels.

To analyze the flow evolution, we constructed the kinetic energy maps from velocity spectra. In Figs. 5(a)–5(c), the energy maps for the pure water, the water with SDS, and the water with SDS and NaCl are respectively shown. The first (horizontal) dimension of each image is a spatial dimension oriented along the vessel axis, 0.9 mm per pixel. The second (vertical) dimension is the number of each measurement in the series of 32 PFG measurements acquired at 20 s intervals. A significant amount of stationary water in the two latter cases made filtering of the stationary signal more difficult, so another series of measurement was performed with a 2 cm slice selection along the vessel, to reduce the stationary signal. For the pure water, high kinetic energy suggests an active coherent flow at the very beginning of sonication, next to the transducer. This coherent flow rapidly disappears near the transducer, migrating to the far end of the vessel. For the water with SDS, the flow is steadier and, except for the first minute, more energetic than that of the pure water during the whole experiment. For the water with SDS-NaCl, the flow is also steady but less energetic than for the other cases.

To separate the possible impact of the counterflow, we extracted positive kinetic energy maps, which include only the positive velocities (not shown). The same tendency was observed: the coherent flow almost disappears for the pure water, is steadier and more uniform along the vessel for the water with SDS, and is uniform but weak for the water with SDS-NaCl.

To confirm these findings, we performed another series of experiments, in which a different slice through the vessel was imaged. The 1.9-cm-thick transverse slice was oriented perpendicularly to the vessel axis and was located at the center of the vessel. The spatial data were acquired across the vessel, top to bottom, with resolution of 0.35 mm. The displacement encoding was the same as before, along the vessel axis. As a result, we acquired data from a slice in the middle of the vessel with velocity sensitivity along the vessel.

The velocity spectra across the transverse slice are shown in Figs. 6(a)–6(c) for the pure water, water with SDS, and water with SDS and NaCl, respectively. The spectra are extracted from the $N=6$ measurement (40 s after the start of sonication). The vertical axis is the velocity dimension, and

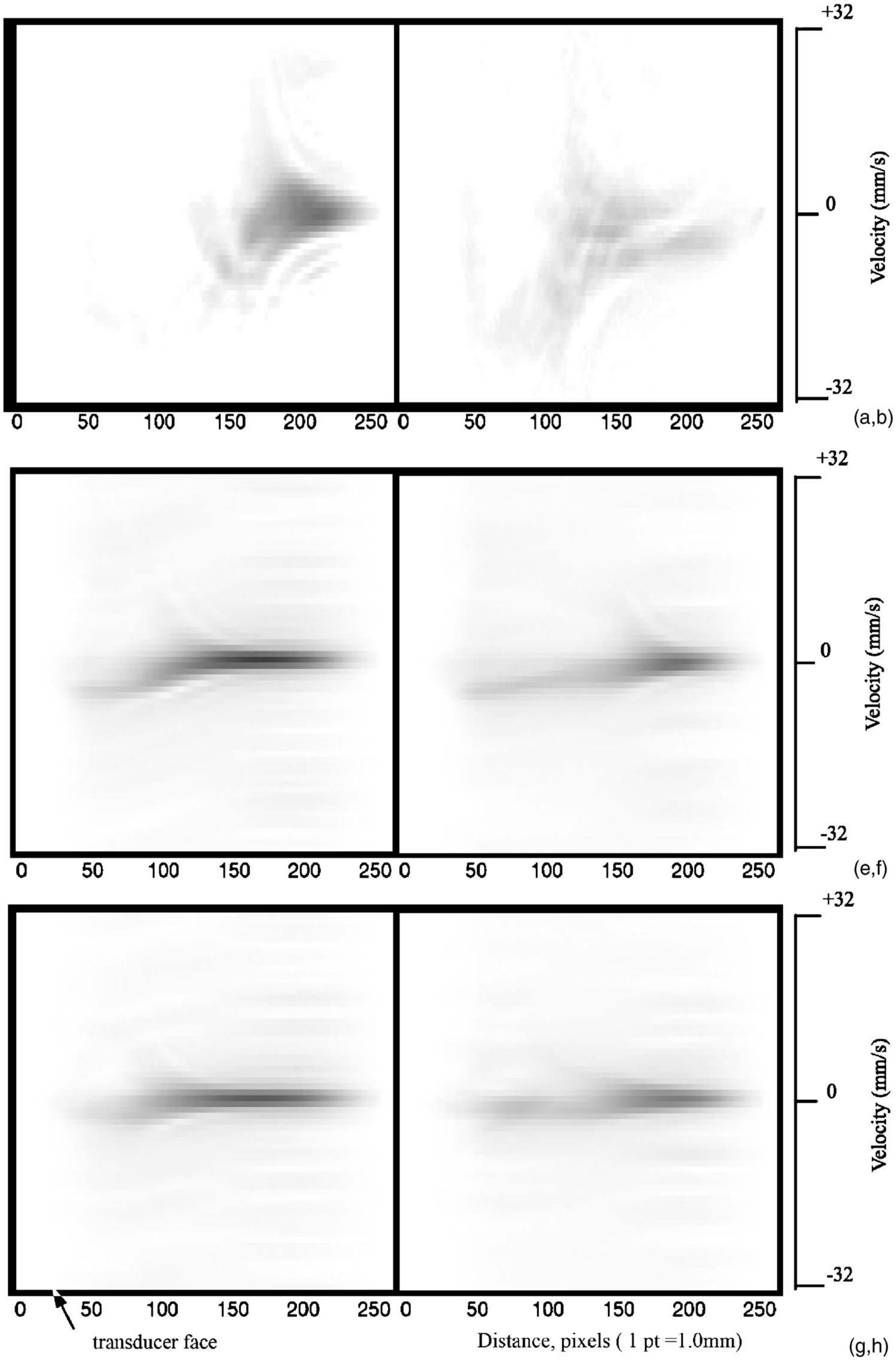

FIG. 4. The velocity spectra of the fifth and sixth measurements for (a), (b) pure water, (c), (d) water with SDS, and (e), (f) water with SDS-NaCl. Horizontal axis is the spatial dimension along the vessel in pixels (1 pixel is 1.0 mm). Vertical axis is the flow velocity along the vessel in mm/s (1 mm/s per pixel), with 0 velocity in the middle and a positive direction away from the transducer (located at point 23).

the horizontal axis is the spatial dimension, at the left corresponding to the bottom of the vessel and at the right corresponding to the top. In all three images, flows have well-characterized velocity profiles through the vessel. The maximum flow velocity in the pure water is 6.5±1 mm/s, while in the samples with SDS and SDS-NaCl the maximum velocities are 28±1 and 7.8±1 mm/s, respectively. This is the moment at which a coherent flow propagates through the slice. On the subsequent measurements (not shown here), the flow coherence is destroyed in the pure water, but is present for the other water samples.

The kinetic energy maps for the transverse slice [shown in Figs. 7(a)–7(c)] support this observation: a more energetic coherent flow is detected in the water with SDS. They also show an unusual behavior of the water with SDS-NaCl: a sharp increase in a flow at later times, about 3–8 min after the start of sonication. The flow location is remarkable, being shifted to the top of the vessel. The velocity spectra at those times are characterized by well-defined velocity profiles, again indicative of a coherent flow in salted water with SDS, when there is no such flow in pure water and a significantly weaker flow in the water with SDS.

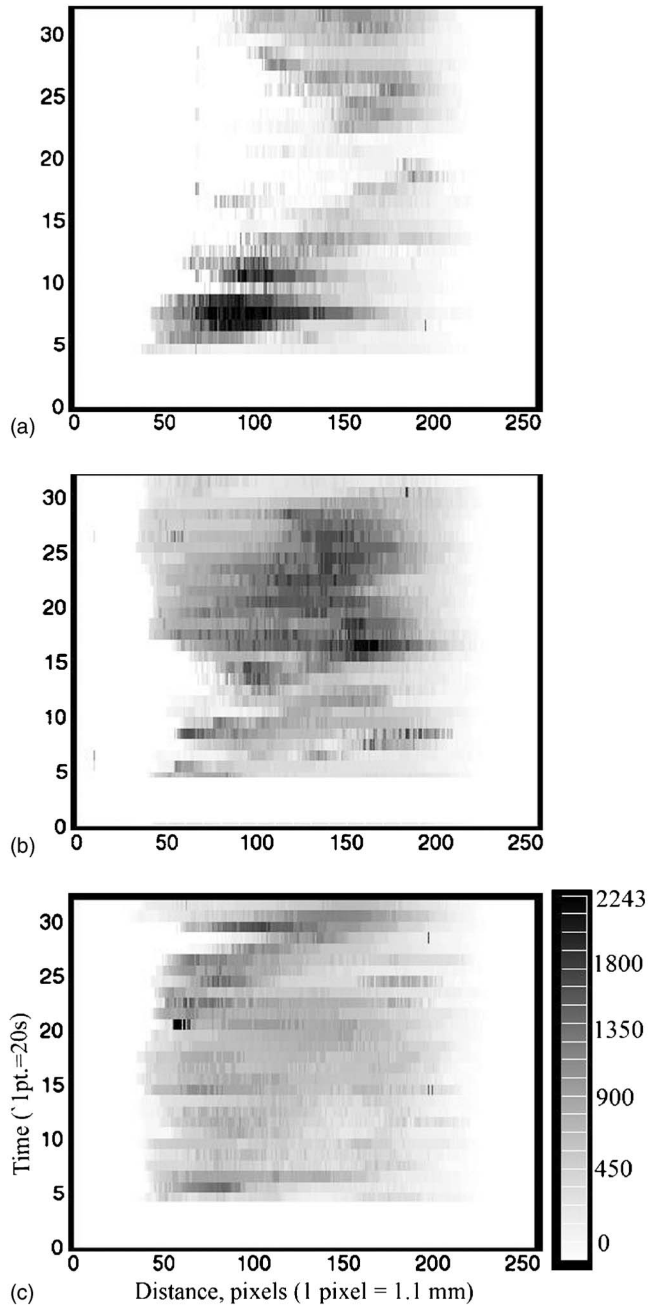

FIG. 5. Relative kinetic energy maps (in a.u.) of the fluids along the vessel axis for (a) pure water, (b) water with SDS, and (c) water with SDS-NaCl. The horizontal axis is distance along the vessel (1 pixel=1.2 mm) as in Fig. 3. The ultrasound transducer was at point 35 and the end of the vessel at point 218. The vertical axis is a time dimension in measurement number from a series of 32. Each measurement takes 20 s and the sonication takes place between measurements 5 and 25 inclusive. The gray scale represents the part of kinetic energy due to motion along the length of the vessel. The energy distribution is increasingly homogeneous, in both space and time, in the series pure water, water-SDS, and water-SDS-NaCl.

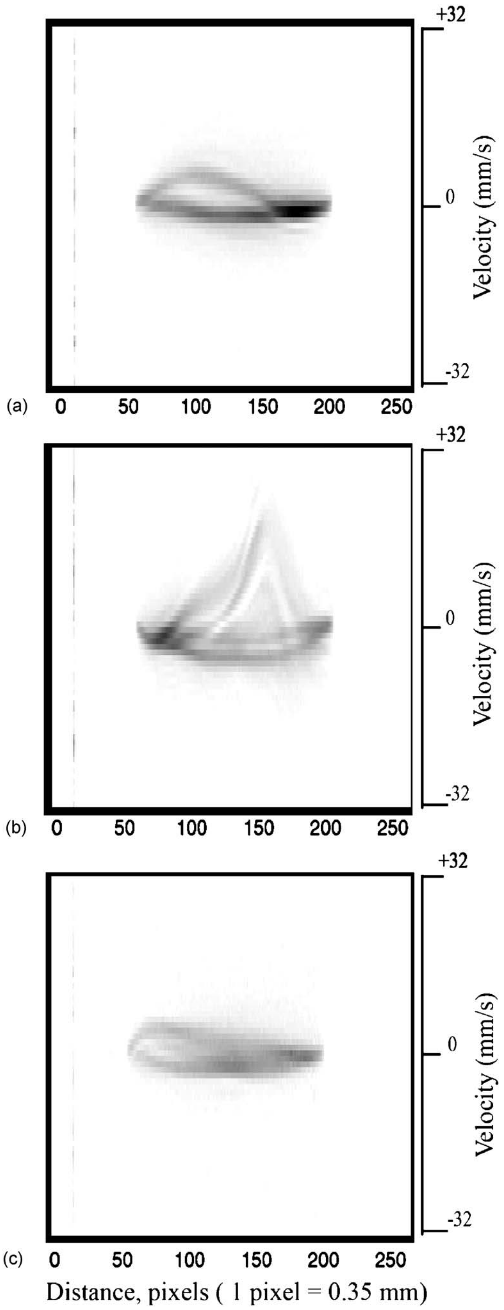

FIG. 6. The velocity spectra of a transverse slice of fluid: (a) pure water, (b) water with SDS, and (c) water with SDS-NaCl. The slice was orthogonal to the length of the vessel, halfway along its length. The spectra were acquired 60 s after the start of sonication (in the eighth measurement). The horizontal axis is distance across the vessel in pixels (1 pixel=0.35 mm). Every row is a profile across the apparatus (in contrast to Fig. 3), from the top of the vessel at pixel 51 to the bottom of the vessel at pixel 200. The vertical axis is the flow velocity, in mm/s, along the vessel length (orthogonal to the slice). Positive velocities are away from the transducer.

We also performed experiments with the displacement encoding directed along the y axis, perpendicular to the vessel axis, for all water samples. Energy maps are shown in Figs. 8(a)–8(c). In this case, the NMR signal is made sensitive to velocities and dispersion in the vertical direction. Such velocities can exist due to circulation near the edges of the vessel, and also between the standing wave nodes and antinodes, known as Rayleigh or outer streaming [1]. However,

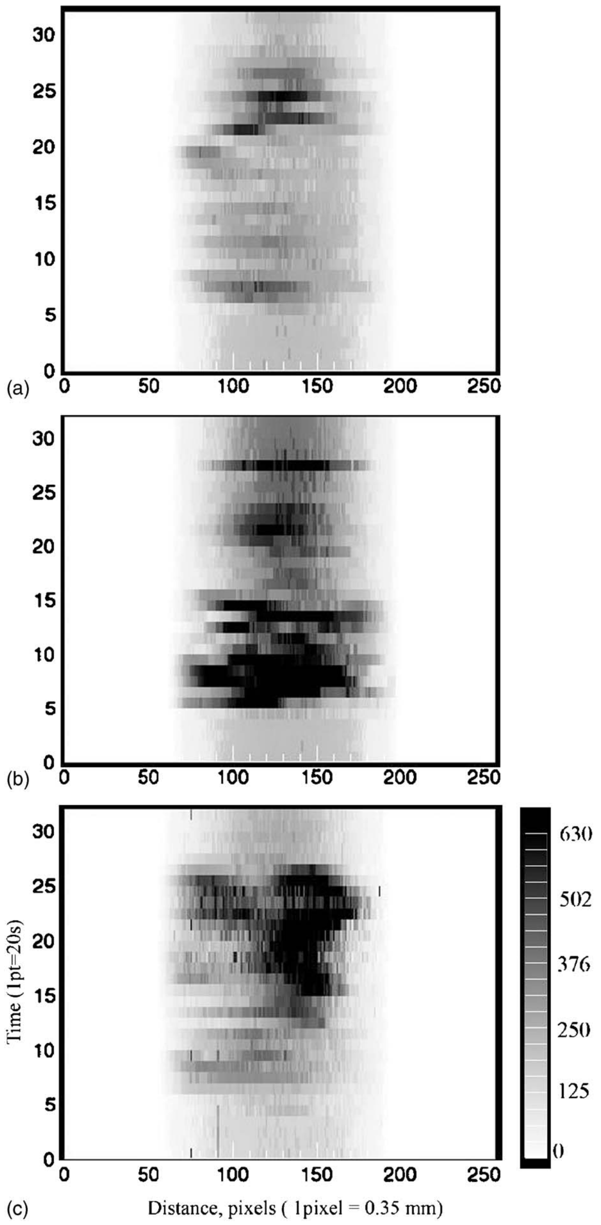

FIG. 7. Relative kinetic energy maps for the transverse slice (as in Fig. 6) across the vessel containing (a) pure water, (b) water with SDS, and (c) water with SDS and NaCl. The horizontal axis is distance across the vessel in pixels (1 pixel=0.35 mm), as in Fig. 6, from the top of the vessel (left, 53) to the bottom (right, 190). The vertical axis is a time dimension in measurement number from a series of 32. Each measurement takes 20 s and the sonication takes place between measurements 5 and 25 inclusive. The gray scale represents the part of kinetic energy due to motion along the length of the vessel. The energy distribution is increasingly homogeneous, in both space and time, in the series pure water, water-SDS, and water-SDS-NaCl.

there was no indication of circulation in pure water, proving that the cavitation completely destroyed coherent flow across the vessel. For samples with SDS and SDS-NaCl, the circulation near both ends of the vessel was evident, being stronger in the former. When the ultrasound is turned off, the circulation in SDS and SDS/NaCL samples temporarily increases.

We did not detect a stable Rayleigh streaming in any water samples. There was a spatial inhomogeneity of velocity spectra for pure water, but the patterns changed with time.

C. Hydrodynamic dispersion measurements and dispersion maps

By "dispersion" here we mean a mechanical hydrodynamic dispersion. Hydrodynamic dispersion consists of both molecular diffusion and kinematic dispersion (mixing caused by microflows) [7], and we measured it in the same way as diffusion, via attenuation of the MRI signal amplitude with increasing gradient strength. In Eq. (2), D becomes the coefficient of hydrodynamic dispersion. In acoustics and optics, however, the word "dispersion" is usually employed to describe the dependence of phase speed on frequency [8], a phenomenon very different from hydrodynamic dispersion.

Our measurement time of 20 s determines our sensitivity to temporal stability of the system under investigation. If the flow field significantly changes during our measurement, the obtained data will be irregular and will not be fitted by the fitting routine, nor will Fourier transformation yield a well-defined velocity spectrum. In such cases, the fitting routine attributed a zero or a negative value to the dispersion coefficient, indicating the temporal instability in that location.

With one-dimensional resolution scheme in our experiments, there is an inevitable averaging of the signal across the vessel. Correspondingly, the measured dispersion coefficient, presented here in units of self-diffusion of water, is an averaged value.

Dispersion maps were obtained for two directions of displacement-encoding gradients. The first direction was horizontal (along the vessel axis), the second direction was vertically upward. Regions of flow instability are seen as noisy regions located in the vicinity of the transducer (Fig. 9). A characteristic feature of the dispersion maps is the propagation of elevated dispersion coefficient (a dispersion front) along the vessel. This dispersion front propagates in bursts, which coincide with bursts on the maps of stationary fluid, and can be related to cavitation propagating along the vessel.

For the pure water, the zone of flow instability covers the whole vessel behind the dispersion front for the total time, with the possible exception of the first measurement, after the activation of sonication. For the water with SDS, the unstable areas are much smaller and realized near the transducer. Unstable areas are absent in water with SDS-NaCl. The elevated dispersion zone is also smaller in water with SDS-NaCl and is reduced toward the end farthest from the transducer. Just as in the energy maps for the transverse slice [Fig. 7(c)], there is an increased activity in the water with SDS-NaCl in the later stages of the measurement: the dispersion coefficient reaches its highest values at rows 22–25 (7 min after the start of sonication).

Maps of dispersion across the vessel (not shown here) show the stochastic displacements in the direction perpendicular to the sound beam. They, too, demonstrate the disper-

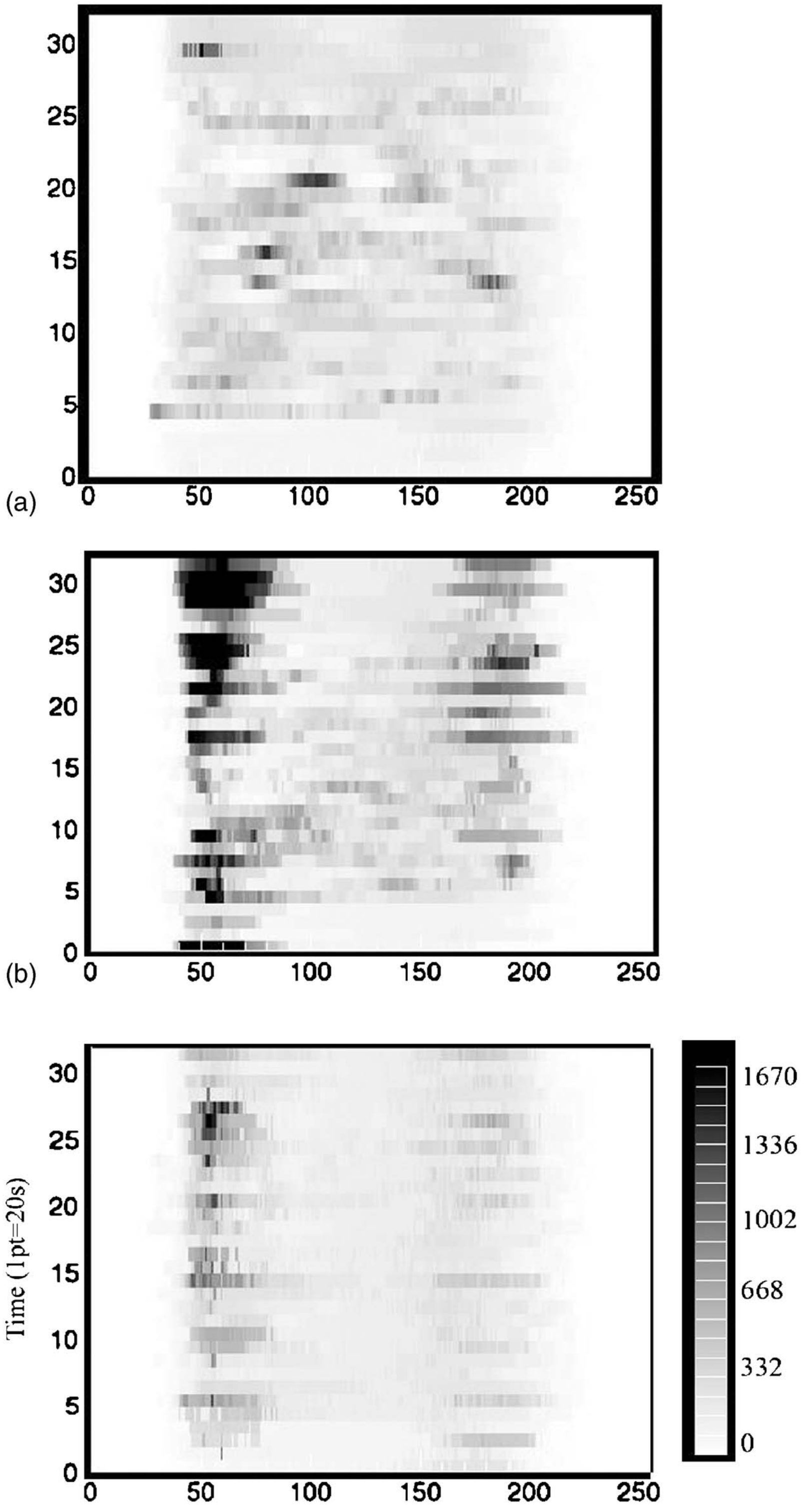

FIG. 8. Relative kinetic energy maps for the part of the kinetic energy contributed by velocity orthogonal to the length of the vessel containing (a) pure water, (b) water with SDS, and (c) water with SDS and NaCl. The horizontal axis is distance along the vessel in pixels (1 pixel =1.2 mm) and each row is, therefore, a profile along the length of the vessel. The transducer is at pixel 41 and the end of the vessel is at pixel 210. The vertical axis is a time dimension, each row corresponding to a separate measurement in a series of 32. The duration of each measurement is 20 s. Sonication is carried out from measurement 5 to measurement 25, inclusive. The measurements are sensitized to motion in the direction orthogonal to the vessel axis. Motion in this direction would occur with circulation of the fluid in the vessel. There is no evidence of any circulation in (a) the pure water. There is a little circulation in (c) water with SDS-NaCL and more in (b) water with SDS. In both cases, the concentration of kinetic energy at the ends of the vessel indicates circulation in a single cell encompassing the entire length of the vessel.

sion front for the pure water, but the front does not span the whole length of the vessel. For water with SDS, the dispersion does not change as much as for the pure water, and the water with SDS-NaCl seems to be mostly unperturbed.

When the maps of dispersion in two directions are compared, a strong anisotropy of dispersion becomes evident for water with addition of SDS: there is virtually no increase in dispersion across the vessel. It can be better seen on the averaged dispersion profiles [Figs. 10(a)–10(c)] obtained from the dispersion maps by summing the PFG measurements from the fifth to 25th (from the start of sonication until its end). For the pure water [Fig. 10(a)], the profiles with dispersion along and across the vessel have comparable values greater than the self-diffusion coefficient of water and maintain a similar spatial structure: broad peaks separated by approximately the wavelength distance. For water with SDS

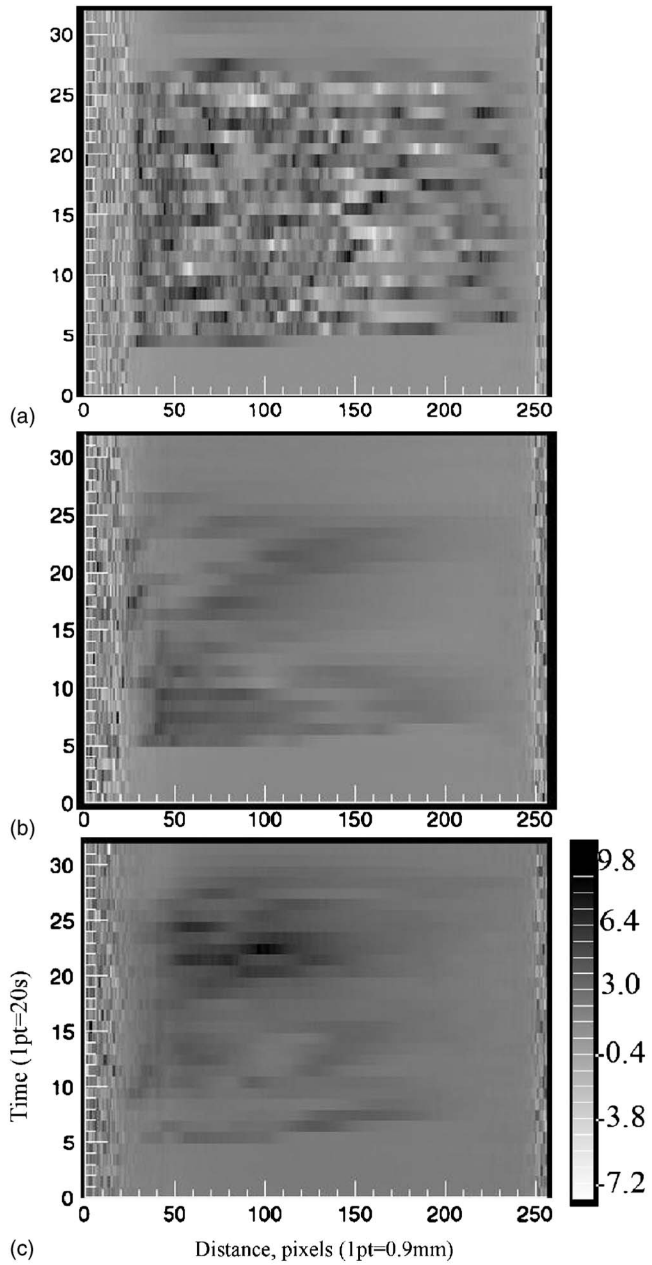

FIG. 9. Maps of the principal component along the vessel length of relative dispersion coefficient in the vessel containing (a) pure water, (b) water with SDS, and (c) water with SDS and NaCl. The horizontal axis is distance along the vessel in pixels (1 pixel $=0.95$ mm). Each row is a profile along the length of the vessel. The transducer is at pixel 15 and the end of the vessel is at pixel 246. The vertical axis is a time dimension, each row corresponding to a separate measurement in a series of 32. The duration of each measurement is 20 s. Sonication is carried out from measurement 5 to measurement 25, inclusive. The gray scale indicates the principal component along the vessel length of dispersion coefficient measured relative to the molecular self-diffusion coefficient of water at 20 °C (2.0×10^{-9} m^2/s).

[Fig. 10(b)], the first three peaks are separated by the half-wavelength distance for the dispersion along the vessel, but all structural features barring a single peak near the transducer are absent. For the dispersion across the vessel, the dispersion coefficient is almost entirely due to the self-diffusion of the water ($D\approx D_{water}$). The profile for water with SDS-NaCl also has several broad peaks for the dispersion along the vessel, and only a single peak next to the transducer for the dispersion across the vessel.

IV. DISCUSSION

A. Acoustic streaming

Acoustic streaming is a steady flow produced by the absorption of acoustic energy and is often used to measure the absorption coefficient of a medium [9]. Acoustic streaming in the submegahertz and megahertz range is important for clinical applications of ultrasound and has been studied extensively, including MRI studies [10]. The absorption coefficient $\alpha\propto\omega^2$ is very small for water at 31 kHz, and an estimated acoustic streaming velocity at such low frequencies, for the employed transducer power, would be several micrometers per second.

We were unable to detect an acoustic streaming in the degassed water. However, streaming was pronounced in all our measurements of nondegassed water samples. Clearly, the presence of gaseous bubbles, which are excellent acoustic energy absorbers, is critical for the observed streaming. When the experiments were performed on the same water sample several times in a row with 5 min interval, the streaming was becoming weaker with every subsequent experiment, indicating a partial degassing of the sample.

Two types of streaming are distinguished in a cavitating fluid: Eckart streaming caused by bulk absorption of acoustic energy by bubbles acting as absorbing agents, and a quasiacoustic streaming caused by radiation pressure acting on the cavitating bubbles [2,11,12]. In a standing wave, radiation pressure causes bubble migration between nodes and antinodes of pressure, depending on their size. The radiation pressure, therefore, is expected to generate a streaming on the half wavelength scale, similar to Rayleigh streaming.

It is still possible, however, that the radiation pressure drop with distance from the transducer, will result in a net force along the vessel, generating a steady flow.

Most probably, both types of streaming are present. Quasiacoustic streaming is characterized by a decelerating flow, while Eckart streaming is characterized by a flow accelerating away from the transducer. Immediately after the start of sonication, all the velocity profiles are decelerating. In the second half of the experiments (from the 15th PFG measurement), there is an accelerating flow in SDS-containing samples.

The dynamics of both types of acoustic streaming should reflect the behavior of cavitating bubbles in the acoustic field. Indeed, our measurements demonstrate that for three water samples (pure water, water with SDS, and water with SDS-NaCl), the acoustic streaming patterns are different. An observed enhancement of streaming by SDS can be explained by the stabilization of the bubbles and reduction of their coalescence.

SDS is known for its effects on the cavitation field, especially on bubble interactions [3,4]. A working hypothesis [4] is that, as the anionic surfactant accumulates at the bubble

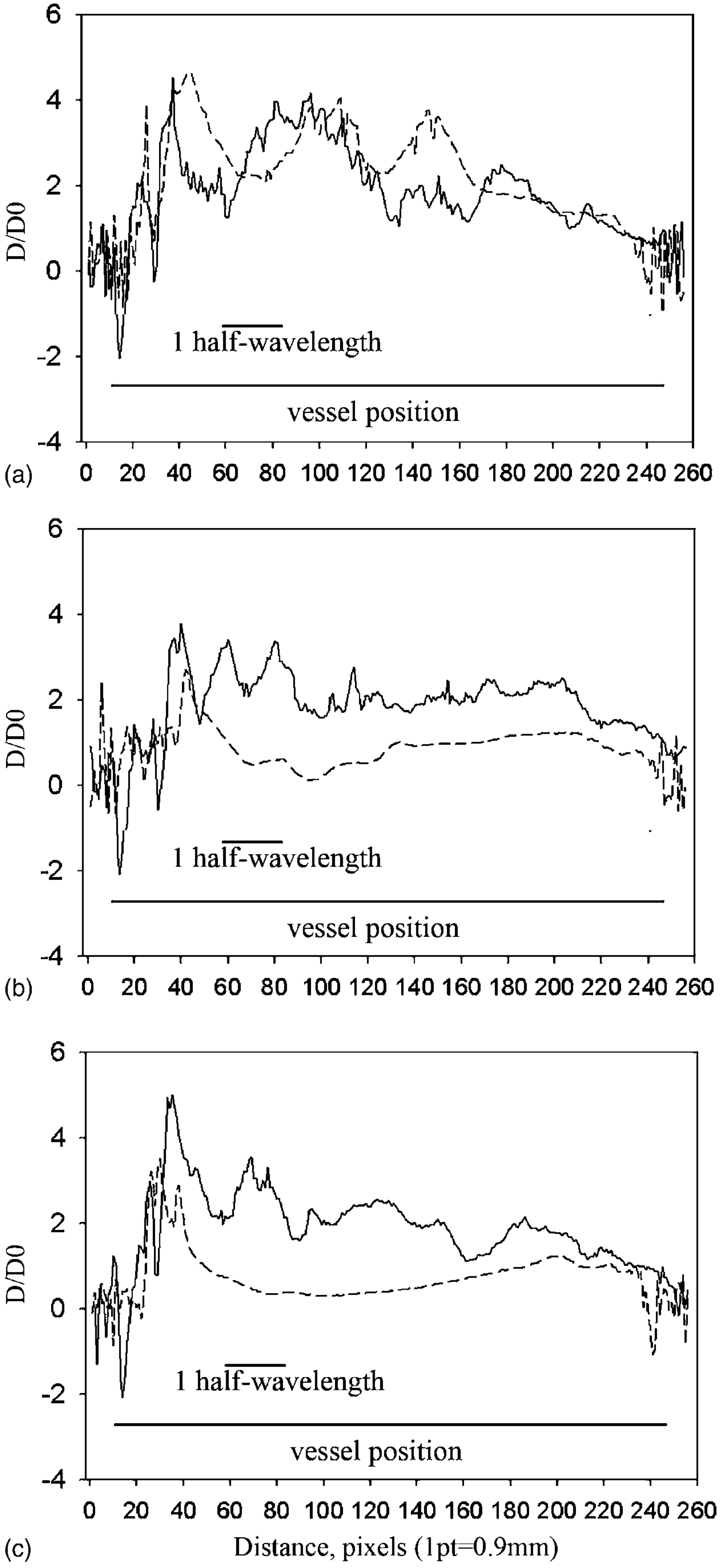

FIG. 10. Maps of the principal component along the vessel length of relative dispersion coefficient in the vessel containing (a) pure water, (b) water with SDS, and (c) water with SDS and NaCl. The maps were summed from the fifth to the 25th measurement (over the sonication interval) to give the solid profile along the vessel length. Any structure visible in this profile persists, therefore, throughout sonication. The horizontal axis is distance along the vessel in pixels (1 pixel=0.95 mm). The transducer is at pixel 15 and the end of the vessel is at pixel 246. The vertical axis shows the principal component along the vessel length of dispersion coefficient measured relative to the molecular self-diffusion coefficient of water at 20 °C (2.0×10^{-9} m^2/s). The broken line is the sum over the same sonication interval of the principal component orthogonal to the vessel length of relative dispersion coefficient. (a) For pure water, both principal components show regions of elevated relative dispersion coefficient, which peak at intervals of roughly one wavelength of the ultrasonic standing wave. (b) For water with SDS, the longitudinal component of dispersion coefficient is elevated in regions which peak roughly one-half wavelength apart. However, the transverse component of dispersion coefficient is uniform along the vessel length. This difference between principal components indicates an anisotropy in the dispersion coefficient. (c) The profiles of principal components of dispersion coefficient for water with SDS and NaCl are similar to those for water and SDS, but the half wavelength structure is not evident. There is, however, some indication of anisotropy in the dispersion coefficient.

interface, the bubbles acquire a negative charge, and the charged bubbles then tend to repel each other. The maximum effect of surfactant addition on sonochemistry was found experimentally to be at [SDS] of 1–3 m*M* [4]. An addition of NaCl cancels the SDS effects, because NaCl screens the electrostatic field, which may permit bubble flocculation if not coalescence.

In our experiments, there are several reasons why stabilization of bubbles by SDS will enhance streaming: reduced degassing, lengthened liftimes of resonant bubbles, and, possibly, an increased drag coefficient.

If the bubbles are stabilized in size, they will not coalesce readily and leave the liquid quickly due to the buoyancy force which is perpendicular to the direction of the sound wave in our case.

Bubble growth and coalescence will also directly affect the main mechanism of Eckart streaming: energy attenuation by the medium. The energy attenuation is strongest for bubbles near the resonant radius, which is 0.1 mm at 31 kHz (using the Minnaert formula [13]). When the number of resonant bubbles reduces, due to their coalescence, the volume force decreases, and the Eckart streaming will be diminished. If the bubbles are stabilized by the surfactant, they will comprise a more stable size distribution, with the resonant bubbles generating the streaming.

For bubbles moving freely through a fluid, there is a significant amount of data on the surfactant stabilization of the bubble surface and, thus, reduction of bubble deformation (for example, [14,15]), with a "marked decrease in terminal velocity" [14] and an increase of the drag coefficient of the bubbles.

With the inception of cavitation, a coherent flow develops in the vessel for all non-degassed water samples. The flow is the strongest in the pure water and weaker in water samples with surfactant. The flow, however, quickly (within 20–40 s) disappears in pure water, as cavitation propagates along the vessel. We think that the turbulence caused by cavitation dominates the steady flow. This transition from laminar to turbulent flow due to cavitation was observed, for example, in [16]. In the case of water with SDS, the flow is more stable, with a pronounced circulation. The surfactant-stabilized bubbles fragment and coalesce less actively, thus they are less destructive of the steady flow.

NaCl did not completely reverse the action of SDS in our experiments. NaCl definitely suppressed cavitation-caused perturbation, according to the maps of stationary fluid (Fig. 3). Streaming in the water with SDS-NaCl was less pronounced than in the water with SDS and resembled the streaming in the pure water. However, about 7 min after the start of sonication, streaming becomes stronger, with well-defined velocity profiles (reflected in the kinetic energy maps) and an increase in the dispersion along the sample (Fig. 9).

There are experimental data [17] for bubbles in flowing noncavitating water that show a decrease in bubble diameter with an increase in ionic strength. One of the explanations proffered by the authors is also that the ionic repulsion between the bubbles in salt water prevents bubble coalescence. In our case, it is possible that, with smaller initial sizes prevailing, the bubble growth takes longer than in case of pure water. When the bubbles approach the resonant bubble size, they will absorb energy and thus produce streaming; however, there is a need for more experimental data to support this explanation.

B. Dispersion

At least two factors can increase the dispersion in cavitating fluid: microstreaming and bubble migration. Microstreaming is caused by cavitating bubbles and is thought to be responsible for an active mixing of the fluid in cavitation fields [18]. The second source of dispersion in the standing wave is the bubble migration between the nodes and antinodes of pressure. The origins of such migration are rectified diffusion that causes bubble growth, and the primary Bjerknes force that attracts bubbles smaller than the resonant size toward and repels larger bubbles away from the nodes.

Bubble migration is expected to affect the dispersion along the direction of the sound wave propagation, i.e., along the principal axis of the vessel in our case. It will generate an anisotropic dispersion. Microstreaming should not have a preferred direction in the bulk of the liquid. Only near the rigid boundaries will the microflows be directed towards the boundaries [18]; this boundary effect can be neglected in our experiments, because most of the detected signal comes from the bulk. Microstreaming will generate an isotropic dispersion in the fluid.

Accordingly, the observed anisotropy of the dispersion for water with SDS and SDS-NaCl can be explained by a reduction of microstreaming in solutions with surfactants. While the dispersion profiles of the pure water show approximately the same locations of zones with high dispersion for displacements both along and across the vessel, the dispersion profiles of water with surfactants show no high-dispersion zones for the displacements across the vessel. The stabilization of bubbles with surfactants reduces bubble fragmentation, decreasing the microstreaming and reducing the isotropic component of dispersion.

The accumulation of bubbles at pressure antinodes, their sonoluminescence and their effects on exposed materials (metal foils, tissues, cells, etc.) have been observed by many authors (see, for example, [18]). The results are usually a characteristic stripe pattern with a separation of a half wavelength.

In our experiments, we did not expect to see such a pattern, because our measurement detects not the bubbles themselves but the dynamics of surrounding fluid. Additionally, our measurement is spatially one dimensional, and, therefore, a severe averaging over the other dimensions is involved. However, we observed high-dispersion zones, with locations different in the pure water and water with SDS and SDS-NaCl (for the dispersion along the vessel). In the pure water, the high-dispersion zones are broad and occupy about a wavelength each. In water with SDS in the vicinity of the transducer, there are three well-resolved peaks separated by a half wavelength. In water with SDS-NaCl, the pattern again resembles that of the pure water. This increase in dispersion (both along and across the vessel) means an active mixing and bubble migration in the pure water: as the bubbles grow larger than the resonant size, they are expelled from the antinodes to the nodes. The localized dispersion in water with SDS might mean an accumulation of smaller, surfactant-stabilized bubbles in antinodes, with the restricted bubble migration due to a slower bubble coalescence.

V. CONCLUSION

In this paper, we applied MRI to measurements of acoustic cavitation. We demonstrate that MRI can provide useful information on the velocity and dispersion in cavitating fluids.

A pronounced streaming and dispersion were observed only in nondegassed water samples and only at ultrasound power above the cavitation threshold. Therefore, both streaming and increased dispersion can be attributed to the presence of cavitation bubbles. If the bubble dynamics are modified, the behavior of surrounding fluid is changed on the macroscale.

The difference in streaming in water and water with SDS is significant. Much stronger streaming in water with the surfactant can be caused by, first, a larger number of stabilized bubbles and, second, a less disruptive cavitation. A modification of bubble dynamics by the surfactant can qualitatively explain the observed difference, but additional work is required to identify the main streaming mechanism.

A difference in dispersion in water and water with SDS was also substantial. The most interesting feature of the dispersion was its anisotropy in water with the surfactant: almost no dispersion increase across the vessel.

Due to the sensitivity of fast MRI methods to the presence of the metal transducer cover, we had to employ a slow imaging method. Spin-echo PFG provided a temporal resolution of 20 s per measurement, which was adequate for the processes in the systems under study, but with only one-dimensional spatial resolution. We are working on an imaging method SPRITE [19–22] with flow-sensitized preparation that will allow us to obtain velocity and dispersion images with two-dimensional spatial resolution within the same time frame.

ACKNOWLEDGMENTS

The authors thank Professor B. J. Balcom and Dr. D. Green for useful discussions and the Natural Sciences and Engineering Research Council of Canada for financial support. The UNB MRI Centre is supported by an NSERC Major Facilities Access Award.

---

[1] W. L. Nyborg, in *Physical Acoustics*, edited by W. P. Mason (Academic Press, New York, 1965), Vol. 2, Part B.

[2] C. Campos-Pozuelo, C. Granger, C. Vanhille, A. Moussatov, and B. Dubus, Ultrason. Sonochem. **12**, 79 (2005).

[3] N. Segebarth, O. Eulaerts, J. Reisse, L. A. Crum, and T. J. Matula, J. Phys. Chem. B **106**, 9181 (2002).

[4] M. Ashokkumar, R. Hall, P. Mulvaney, and F. Grieser. J. Phys. Chem. B **101**, 10845 (1997).

[5] E. O. Stejskal and J. E. Tanner, J. Chem. Phys. **42**, 288 (1965).

[6] P. T. Callaghan, *Principles of Nuclear Magnetic Resonance Microscopy* (Clarendon Press, Oxford, 1993).

[7] J. D. Logan, *Transport Modeling in Hydrogeochemical Systems* (Springer, New York, 2001).

[8] M. F. Hamilton, Yu. A. Il'inskii, and E. A. Zabolotskaya, in *Nonlinear Acoustics*, edited by M. F. Hamilton and D. T. Blackstock (Academic Press, New York, 1988).

[9] J. E. Percy and J. Lamb, Proc. R. Soc. London, Ser. A **226**, 43 (1954).

[10] H. C. Starritt, C. L. Hoad, F. A. Duck, D. K. Nassiri, I. R. Summers, and W. Vennart, Ultrasound Med. Biol. **26**, 321 (2000).

[11] H. Mitome, in *Advances in Nonlinear Acoustics*, edited by H. Hobaek (World Scientific, Singapore, 1993).

[12] S. Nomura, K. Murakami, and Y. Sasaki. Jpn. J. Appl. Phys., Part 1 **39**, 3636 (2000).

[13] M. Minnaert. Philos. Mag. **16**, 235 (1933).

[14] R. Clift, J. R. Grace, and M. E. Weber, *Bubbles, Drops, and Particles* (Academic Press, Boston, 1978).

[15] S. S. Alves, S. P. Orvalho, and J. M. T. Vasconcelos, Chem. Eng. Sci. **60**, 1 (2005).

[16] S. Nomura, K. Murakami, and M. Kawada, Jpn. J. Appl. Phys., Part 1 **41**, 6601 (2002).

[17] E. S. Winkel, S. L. Ceccio, D. R. Dowling, and M. Perlin, Exp. Fluids **37**, 802 (2004).

[18] T. G. Leighton, *The Acoustic Bubble* (Academic Press, San Diego, 1994).

[19] B. J. Balcom, R. P. MacGregor, S. D. Beyea, D. P. Green, R. L. Armstrong, and T. W. Bremner, J. Magn. Reson., Ser. A **123**, 131 (1996).

[20] I. V. Mastikhin, B. J. Balcom, P. J. Prado, and C. B. Kennedy, J. Magn. Reson. **136**, 159 (1999).

[21] M. Halse, J. Rioux, S. Romanzetti, J. Kaffanke, B. MacMillan, I. V. Mastikhin, N. J. Shah, E. Aubanel, and B. J. Balcom, J. Magn. Reson. **169**, 102 (2004).

[22] S. Hatanaka, K. Yasui, T. Kozuka, T. Tuziuti, and H. Mitome, Ultrasonics **40**, 655 (2002).